Journal of Porous Materials
https://doi.org/10.1007/s10934-024-01589-6

SBA-15 with short-sized channels modified with Fe_2O_3 nanoparticles. A novel approximation of an efficient adsorbent for As removal in contaminated water

Viviana Palos-Barba[1] · Rufino Nava Mendoza[2] · Beatriz M. Millán-Malo[1] · Manuel Aguilar-Franco[1] · Carmen Peza-Ledesma[1] · Eric M. Rivera-Muñoz[1]

Abstract
The urgent need for technologies to ensure health standards, as per the Sustainable Development Goals established by the United Nations, has prompted research into addressing human health problems associated with chemical contaminants in air, water, and soil. Heavy metals, particularly arsenic, pose significant health risks, with millions of people worldwide exposed to concentrations exceeding recommended limits. Nanostructured materials, including ordered mesoporous substrates such as SBA-15, have shown promise for arsenic removal due to their high surface area and pore characteristics. This study aimed to synthesize a silica mesoporous material with reduced pore channel length to enhance surface area and active sites, thereby improving arsenic removal efficiency. By exploring various surfactant-to-silica precursor ratios, a suitable value was identified to promote the production of shortened SBA-15 particles. These shortened pore channels facilitated the dispersion of iron oxide nanoparticles (Fe_2O_3) on the SBA-15 surface, resulting in an effective adsorbent that achieved over 95% arsenic removal. The combination of the modified SBA-15 substrate and Fe_2O_3 nanoparticles demonstrated high efficiency in arsenic removal from aqueous effluents, offering a promising solution to address water pollution and associated health risks.

Keywords SBA-15 · Arsenic · Adsorption · Fe_2O_3 · Nanoparticles · Porous

1 Introduction

According to the Sustainable Development Goals established in 2015 by the United Nations, there is an urgent need for technologies to ensure the health standards for all societies around the world [1, 2]. Human health problems have been directly associated with the presence and concentration of chemical contaminants in air, water, and soil, causing millions of deaths every year [3]. In the context of water pollution, heavy metals are of great importance due to their toxicity and their relatively low concentration in water bodies; a fact that makes difficult and expensive their removal. Heavy metal separation from aqueous effluents, however, has been approached using several technologies; being reverse osmosis, filtration, ion exchange, and adsorption the most effective [4]. In this context, arsenic is one example of a relevant pollutant that poses important health problems in México and in the rest of the world [5–8]. Recent studies, for instance, have estimated that over 140 million people around the world drink water with higher concentrations of arsenic than that corresponding to the limit recommended

✉ Eric M. Rivera-Muñoz
emrivera@fata.unam.mx

Viviana Palos-Barba
viviana.pb@uaq.edu.mx

Rufino Nava Mendoza
rufino@uaq.mx

Beatriz M. Millán-Malo
bmillan@fata.unam.mx

Manuel Aguilar-Franco
franco@fata.unam.mx

Carmen Peza-Ledesma
cpeza@fata.unam.mx

[1] Centro de Física Aplicada y Tecnología Avanzada, Universidad Nacional Autónoma de México, A.P. 1-1010, Querétaro, 76000 Querétaro, Mexico

[2] División de Investigación y Posgrado, Facultad de Ingeniería, Centro Universitario, Universidad Autónoma de Querétaro, 76010 Querétaro, Mexico

Published online: 13 April 2024

by the World Health Organization (WHO) [9]. In México, the presence of arsenic in groundwater in regions like the states of Chihuahua, Durango, and Zacatecas represents a significant health threat, with an estimated 9 million people consuming water from contaminated sources with higher concentrations than the limit proposed by the WHO, which is why research work has emerged that seeks to facilitate the detection or quantification of arsenic in water [10, 11]. The main cause of arsenic poisoning is ingesting water with high levels of arsenic and consuming foods that have been prepared with contaminated water [12]. Health problems related to arsenic depend largely on the time of exposure, the species of arsenic with which one came into contact, and the concentration. The most common effects are skin damage and the development of cancer, however, relationships of arsenicism with respiratory, cardiac, and gastrointestinal problems, nephrotoxicity, and neurotoxicity have been reported [12, 13].

Carbon nanotubes with iron oxide nanostructures have been used to absorb arsenic from contaminated water due to their surface-to-volume ratio [14], Mn–Fe layered double hydroxide has been tested as an adsorbent from acid mine drainage [15] and other alternatives based on inexpensive materials [15] have shown relevant adsorption capacities to remove arsenic from water. Due to their low cost, simple manufacturing, and enhanced properties, nanostructured materials are being studied for arsenic removal [16–19]. Among these, adsorbents like the ordered mesoporous substrates such as MCM-41 (Mobil Composition of Matter No. 41) and SBA-15 (Santa Barbara Amorphous No. 15) have been used due to their specific morphological properties such as high surface area and, wide pore diameter and high volume [20–24]. These features provide a large number of sites to locate metals, amines, and other species capable of reducing/oxidizing chemicals and adsorbing ions from aqueous effluents [25–28]. The morphology of these mesoporous materials, on the other hand, can be improved by changing the silica precursor, the surfactant ratio, and the co-solvent nature during the synthesis procedure. As a consequence, different forms and shapes such as fibers, road-like figures, spheres, and platelet mesoporous materials, can be readily obtained [29–31]. In this way, conventional SBA-15 specimens with a reduction in the length of the average particle could enhance diffusion processes through the mesopore channels, to promote the contact between the contaminated water and the adsorbent nanoparticles.

In this context, the goal of this work was to synthesize a silica mesoporous material, favoring a reduced length of pore channels, to increase the surface area within the pores and active sites. This would result in higher efficiencies of As removal from aqueous effluents. For this purpose, several ratios of the surfactant to silica precursor were explored to find a suitable value that promotes a short-length SBA-15 particle. It is expected that the shorter pore channels thus obtained, could facilitate the dispersion of adsorptive nanoparticles on its surface as well as the diffusion of contaminated water. Therefore, a length-reduced particle was used as a support to incorporate iron oxide nanoparticles (Fe_2O_3) on its surface. Since these nanoparticles are known to be effective in adsorbing arsenic [32–35], the combination of the SBA-15 substrate and the Fe-based nanoparticle, resulted in an effective adsorbent that achieved over 95% As removal, which is a very high value when compared with currently available adsorption systems using iron oxide [25–30].

2 Experimental

2.1 Synthesis of the SBA-15 substrate

The adsorbents consisted of a modified SBA-15 support material, starting from a sol-gel method reported elsewhere [36]. In this procedure, 4.8 g of the structural directing agent Pluronic P123 (PEG-PPG-PEG, av. Mn ~ 5800, Sigma Aldrich) were dissolved in a solution of 112.5 ml of deionized water and 75 ml of 4 M hydrochloric acid under constant stirring at 35 °C. Then, 8 ml of a silica precursor, tetraethyl orthosilicate (TEOS, Sigma Aldrich, 98%), were added dropwise to the solution and the mixture was kept under stirring for 24 h at the same temperature. After this, a gel is formed, and it is transferred to a polypropylene bottle to start the aging step at 80 °C for an additional 24-h period without stirring. The obtained precipitate was washed with deionized water and then filtered to finally let dry at 110 °C and calcined at 550 °C for 4 h. To study the effect of the silica precursor/surfactant ratio on the textural properties of the SBA-15, several modifications were made during the synthesis process. Once an improved SBA-15 material was found, it was selected for its potential as an adsorbent for arsenic removal.

2.2 SBA-15 surface modification with Fe_2O_3 nanoparticles

The enhanced SBA-15 was modified on its surface with iron oxide Fe_2O_3 nanoparticles using ferric chloride hexahydrate ($FeCl_3{\cdot}6H_2O$ Meyer, 97%) as the iron precursor. First, four solutions were prepared with 2, 3, 4, and 5 weight percentages of Fe_2O_3. Then, the wet incipient

impregnation procedure [37] was followed to obtain homogenous wet powders. After this, the solids were dried at 110 °C for 18 h and calcined at 550 °C for 4 h to obtain the adsorbents.

2.3 Adsorbents characterization

The textural properties of the SBA-15 substrate and the adsorbents were obtained by N_2 physisorption at 77 K with an Autosorb-IQ^2 instrument (Quantachrome Instruments). The specific surface area was calculated with the Brunauer–Emmett–Teller (BET) method [38] and the pore size distribution using the Barrett–Joyner–Halenda (BJH) method [39]. Scanning transmission electron microscopy (STEM) was performed to get information about the morphology of the materials, using a Nanotech TEM JEOL JEM 2200FS+CS microscope. Photoemission experiments were performed by a SPECS high-resolution X-ray photoemission spectrometer to identify the adsorbent composition and the chemical state of its elements. To confirm the pore arrangement of the modified SBA-15 materials, the adsorbents were analyzed by low-angle X-ray diffraction (XRD) with an Ultima IV Rigaku diffractometer. To identify the crystalline phase for the iron oxide present in the adsorbents, XRD patterns were recorded with a D8 Advance Bruker instrument and validated with High-Resolution Transmission Electron Microscopy (HR-TEM) with a JEOL JEM-ARM200F microscope. The presence of Fe_2O_3 was verified through the vibronic response of the molecular bonds in a Labram-Dior Micro-Raman spectrometer. The semi-quantitative analysis was made with an S2 PUMA Bruker spectrometer to corroborate the amount of iron oxide successfully attached to the substrate material. To obtain information about the surface charge of the adsorbents, the zeta potential was measured using a Zetasizer (Nano-ZS) Malvern Instrument. Fourier Transform Infrared Spectroscopy was conducted to analyze the chemical bonds in samples before and after the arsenic adsorption.

2.4 Adsorption tests

The adsorption performance of the $x\%Fe_2O_3$/SBA-15 adsorbents for As was evaluated using a batch reactor with constant stirring for 60 minutes. Three main factors were studied for these adsorptions: the initial concentration of arsenic in the solutions, assessing 10 and 5 ppm; the amount of Fe_2O_3 in the adsorbents, starting from 2.0 to 5.0 wt%; and the pH of the solutions, natural pH of 2 from the prepared solution and neutral pH of 7 adjusting with HCl. The initial solutions were prepared using deionized water and an arsenic standard (Karal, 1000 ppm). For each test, 0.275 g of the adsorbent was placed in the corresponding arsenic solution at room temperature, and then the suspension was filtered. The atomic absorption spectroscopy (AAS) technique was employed to determine the final concentration of arsenic according to the ISO 17378-2 standard using a Varian AA-240FS Spectrometer [40]. The calculation of the arsenic removal capacity was determined as a percentage (% As Removal), according to the following equation (Eq. 1), where C_0 refers to the initial concentration of arsenic in the solution, and C corresponds to the final concentration.

$$\%\,\text{As removal} = \frac{C_0 - C}{C_0} \times 100$$

To understand the adsorption kinetics of trivalent arsenic, the adsorption of As(III) was studied at an initial concentration of 0.5 ppm at a pH value of 2 and at room temperature. Samples of the solution were extracted at time intervals ranging from 5 to 210 min and subsequently filtered and analyzed using atomic absorption spectroscopy.

The performance of the adsorbents was evaluated to determine the adsorption model that best fits the interaction of the systems under study. The adsorption capacity of the best-performing material was evaluated at initial arsenic concentrations ranging from 0.025 to 0.5 mg/L, to assess the adsorption capacity at concentrations close to the maximum limit allowed by national and international standards. The adsorption isotherms were evaluated according to the Langmuir, Freundlich, and Redlich–Peterson models to determine the best fit that explains the adsorption mechanism.

3 Results and Discussion

3.1 Adsorbent Preparation and Characterization

3.1.1 Short-Sized SBA-15 Substrate

As it was previously mentioned, the surface chemistry characteristics, as well as the morphology features of SBA-15, are closely related to the proportion of silica precursor and the surfactant applied in the synthesis. In this way, it is expected that by making the silica precursor the limiting reagent in the synthesis (by reducing its quantity at the sol step), TEOS would be insufficient to completely coat the directing structure given by the surfactant. Following this idea, four different silica precursor-surfactant (TEOS:P123) ratios (ranging from 0.97 to 2.72) were tested for the synthesis of the SBA-15 matrix. While SBA-15c and SBA-15l correspond to the samples obtained using the smallest and

Table 1 Effects in the textural properties from the silica precursor/surfactant ratio variations during the SBA-15 synthesis

TEOS:P123 ratio	Hysteresis/porous	Surface area (m^2/g)	Pore diameter (nm)
2.72 SBA-15l	H2 disordered pores	759	4.3
2.14 SBA-15	H1 well-defined cylindrical channels	817	5.6
1.55 SBA-15c	H1 well-defined cylindrical channels	1235	5.6
0.97 SBA-15mc	H4 narrow pores and micropores	199	3.4

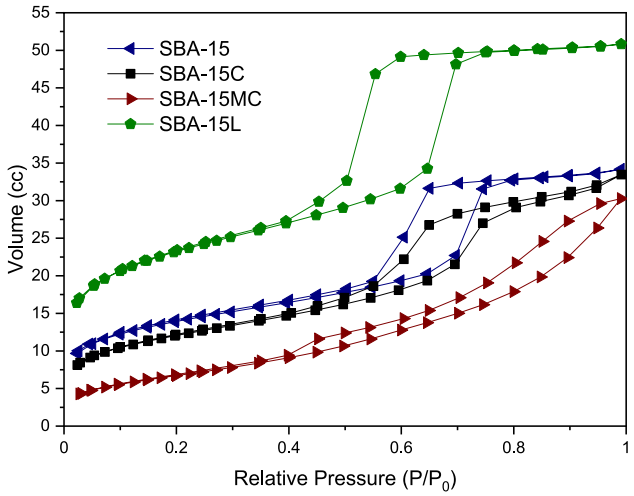

Fig. 1 Adsorption–desorption isotherms for the SBA-15 synthesis variations

the largest quantities of TEOS explored, the reference sample SBA-15, was prepared by using the most common ratio (2.14). The textural properties of these four materials were assessed as described in the experimental section and the resulting data is summarized in Table 1. Inspection of the relevant information shows that all the surveyed materials are characterized by a type IV isotherm (see Fig. 1) [41]. The results also show that the largest increase in the volume of the precursor during the synthesis (SBA-15l) results in an H2-type hysteresis loop that points to a disordered porous arrangement. The smallest ratio of precursor-surfactant on the other hand (SBA-15mc), gives rise to an H4-type hysteresis loop, that suggests micro-sized narrow pores. It is also interesting to note that while the SBA-15 and SBA-15c materials show H1 hysteresis loops that indicate well-defined cylindrical pore channels [42], the largest normalized surface area was observed for a TEOS:P123 ratio of 1.55.

As previously mentioned in the experimental part, the morphology of the reference SBA-15 and the SBA-15c materials was analyzed using STEM. From the resulting images, pore channels can be readily observed in Fig. 2a and d for SBA-15 and SBA-15c, respectively; which confirmed the information provided by the hysteresis loops. The hexagonal pore arrangement typical of the SBA-15 can also be observed in Fig. 2b and e, along with the pore diameter that lies within the range of mesopores [43]. Inspection of the images in Fig. 2c and f, also reveals that the precursor to tensoactive ratio excerpts an almost negligible effect on the dimension of the pore diameter compared to that observed for the length of the pore.

The results of the XPS analysis, as shown in Fig. 3a, indicate the presence of both silanol and silicone oxygen bonds in the O 1*s* region. Specifically, the deconvolution of the oxygen peak revealed binding energy values of 533.0 and 532.3 eV for silanol and silicone oxygen bonds, respectively. Additionally, the presence of these bonds is evident in the Si 2*p* region, as shown in Fig. 3b. The deconvoluted peaks correspond to the silicone oxygen bond at 106.6 eV and silanol bond at 102.8 eV. The presence of silanol groups on the surface of SBA-15 is essential for the incorporation of iron oxide species. The silanol groups provide active sites on the surface, including the inner surface of the pore channels [44].

3.1.2 Fe_2O_3/SBA-15c characterization

From the synthesis characterization described in the previous section, the SBA-15c sample (which is characterized by longer pore channels and a proportional increase in surface area when compared to the standard SBA-15 adsorbent material) was chosen as an adsorbent substrate for Fe_2O_3 nanoparticles that, as it is well known, are particularly effective as As adsorption sites. With the pore filling impregnation method, loads of 2, 3, 4 and 5% by weight of ferric oxide were added. Subsequently, N_2 physisorption analysis was performed at 77 K to evaluate the textural properties of the adsorbent materials. According to pore diameter in Table 2, the incorporation of ferric oxide caused a decrease in the pore size of the support material, which indicates that a portion of the ferric oxide particles are being placed

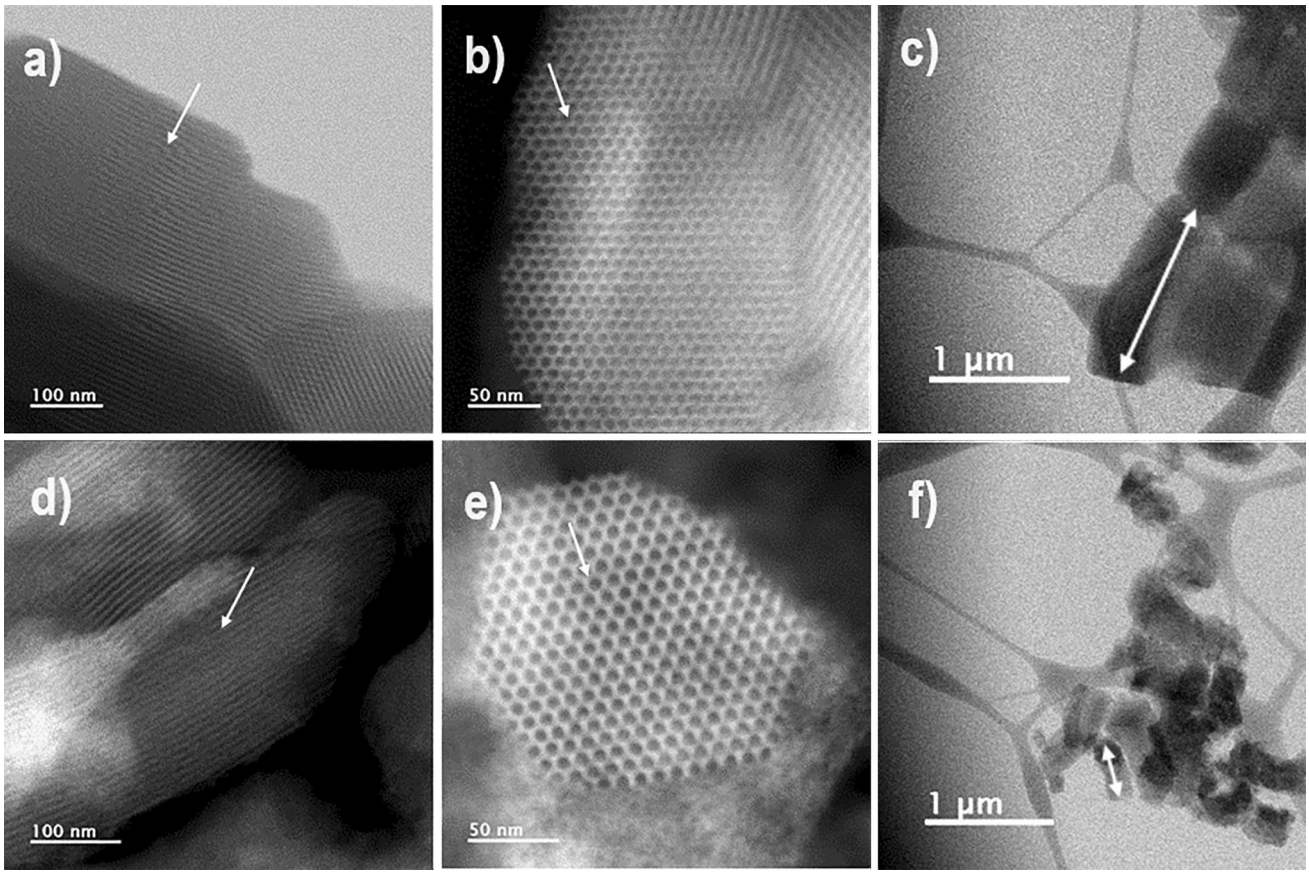

Fig. 2 Scanning Transmission Electron Microscopy for SBA-15 materials: **a** and **d** pore channels for SBA-15 reference and modified SBA-15, respectively, **b** and **e** hexagonal pore arrangement for SBA-15 reference and modified SBA-15, respectively, and **c** and **f** particle length for SBA-15 reference and modified SBA-15, respectively

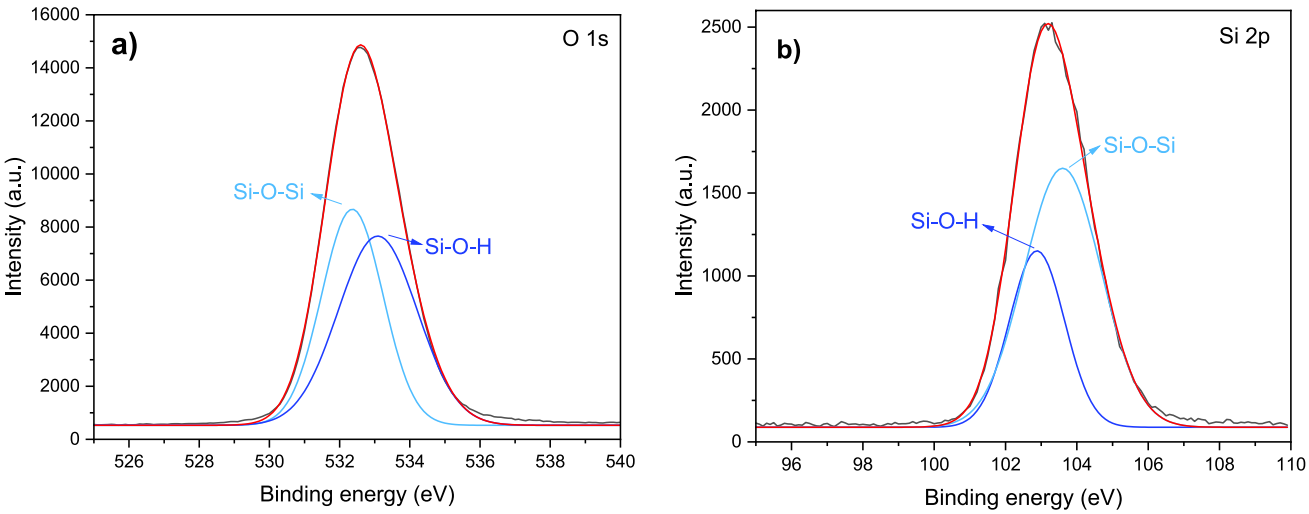

Fig. 3 XPS spectra for short-sized SBA-15 in **a** O 1*s* and **b** Si 2*p* regions

Table 2 Pore diameter of prepared adsorbents

Sample	Pore diameter (nm)
SBA-15c	5.64
2% Fe_2O_3/SBA-15c	4.95
3% Fe_2O_3/SBA-15c	3.43
4% Fe_2O_3/SBA-15c	3.42
5% Fe_2O_3/SBA-15c	4.93

inside the pores until saturation is reached. As a result of this saturation, the average pore diameter onwards 5% Fe_2O_3 loading corresponds to the measurement of larger pores. Following the iron oxide impregnation steps described in the experimental section, low-angle X-ray diffraction patterns were recorded to assess the density and arrangement of the adsorbed metallic oxide nanoparticles on the SBA-15c substrate. From the corresponding experimental data in Fig. 4, hexagonal symmetry (p6mm) could be identified from the (100), (110), and (200) indexes in good agreement with the low-angle XRD SBA-15 patterns published in the literature [45, 46].

XRD patterns from SBA-15c substrates modified with different amounts of Fe_2O_3 are shown in Fig. 5. In all cases, Bragg reflections are observed in 2θ at 24.1° (012), 33.11° (104), 35.61° (110), 40.83° (113), 49.41° (024), 54.00° (116), 57.50° (122) and 62.38° (214), corresponding to the hematite phase α-Fe_2O_3 (PDF#33-0664). These results also show that although the 2% Fe_2O_3 nanoparticle proportion sample seems to produce weak reflections, the main signals (012) and (104) can be seen in the diffractogram.

Following the hematite diffraction pattern, high-resolution TEM images (HRTEM) presented in Fig. 6 confirm the presence of the alpha phase of iron oxide in the SBA-15c material. Fig. 6a displays the characteristic pore channels of SBA-15, while Fig. 6b reveals the crystallinity of

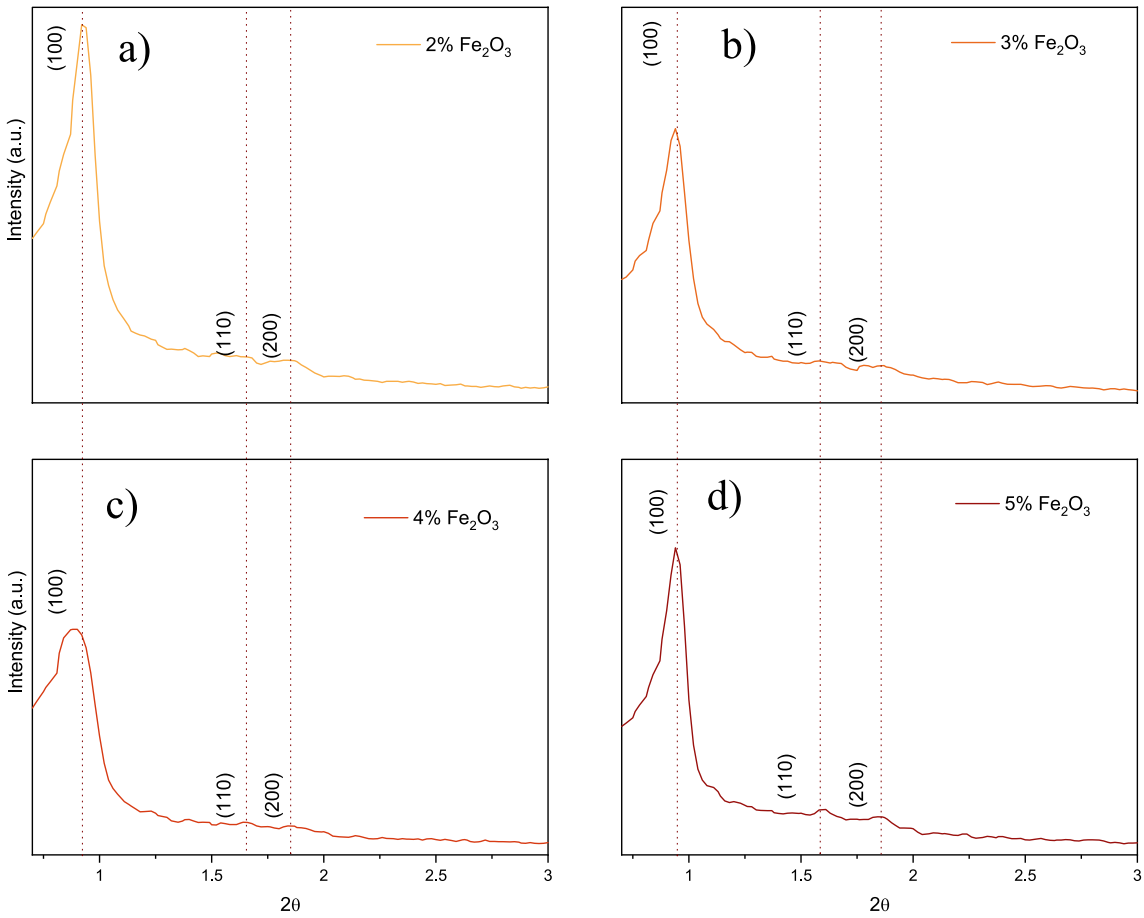

Fig. 4 Low angle X-ray diffraction patterns for the adsorbents: **a** 2%Fe_2O_3/SBA-15, **b** 3%Fe_2O_3/SBA-15, **c** 4%Fe_2O_3/SBA-15, and **d** 5%Fe_2O_3/SBA-15. The dots mark the Bragg reflections corresponding to the hexagonal symmetry

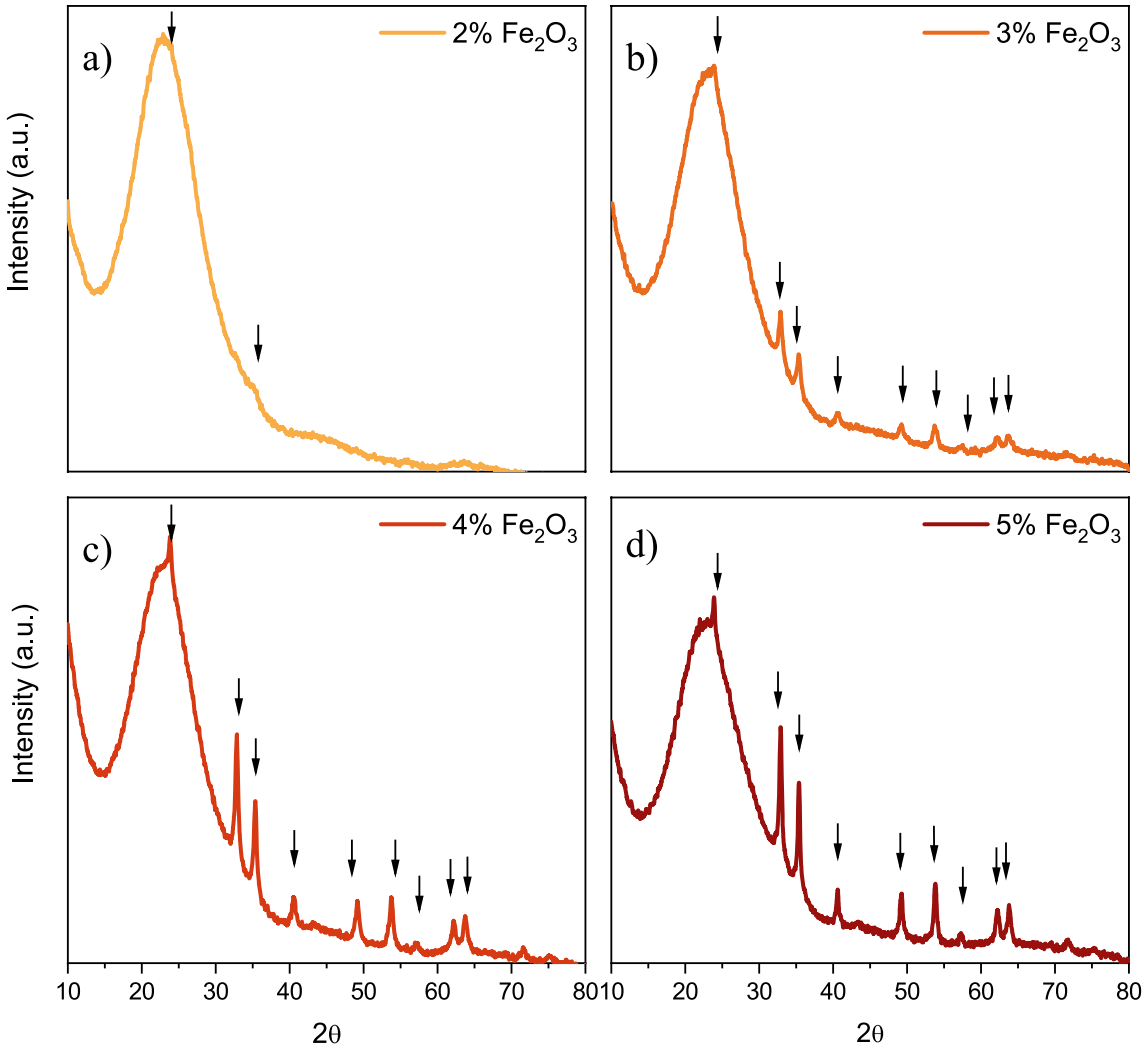

Fig. 5 X-ray diffraction patterns for the adsorbents with 2.0 to 5.0 wt% Fe_2O_3, from **a** to **d** respectively. The arrows show the Bragg reflections corresponding to the hematite phase α-Fe_2O_3

the hematite nanoparticles within the pores. A set of lattice planes with a d-spacing of 2.68 nm corresponding to the (104) plane of the α-Fe_2O_3 phase (PDF#33-0664) can be observed. This confirms that the iron oxide nanoparticles characterized in the SBA-15 material correspond to the α-Fe_2O_3 phase.

The vibronic response of the molecular bonds of the adsorbents, on the other hand, was analyzed using Raman spectroscopy. In this way, Fig. 7 shows the characteristic phonon response of hematite which peaks at 227 and 494 cm^{-1} of the A_{1g} mode, and signals at 245, 292, 299, 409, and 609 cm^{-1} corresponding to the E_g mode, can be observed [47, 48], This assessment validates the experimental calcinating step at 550 °C which does selectively produce α-Fe_2O_3.

The quantity of iron oxide that could be adsorbed on the SBA-15c matrix was evaluated using a semi-quantitative approach through X-ray fluorescence experiments. From the results shown in Table 3, it is possible to conclude not only that the estimated concentration of Fe_2O_3 matches the theoretical

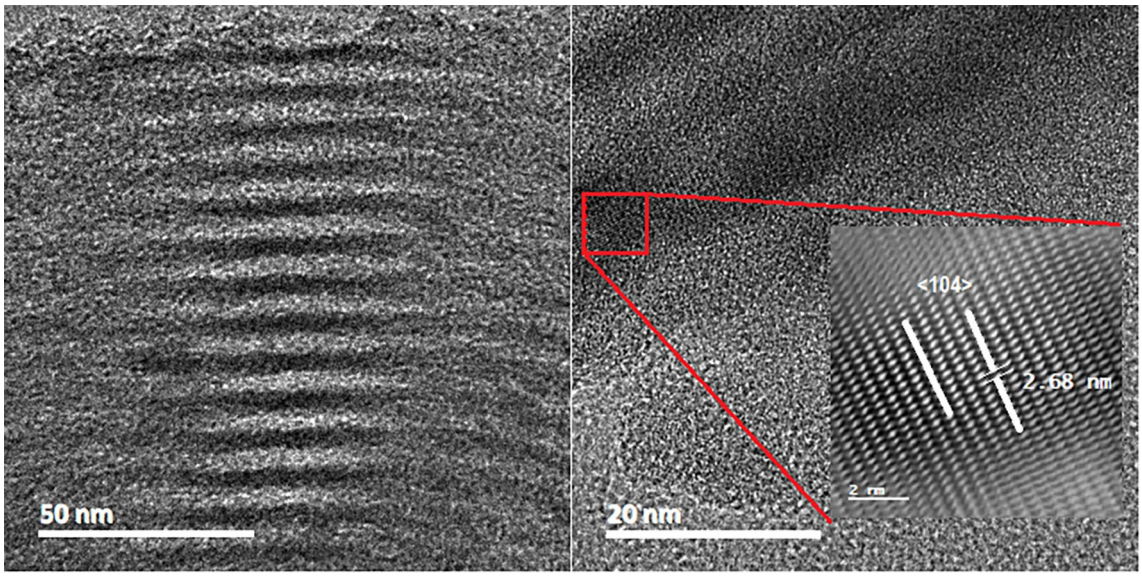

Fig. 6 HRTEM images of α-Fe_2O_3 nanoparticles inside the SBA-15c pore channels

percentage incorporated into the mesoporous SBA-15 matrix, but also that traces of the iron oxide precursor ($FeCl_3 \cdot 6H_2O$) could be identified from the Cl related signal.

The zeta potential plot of the freshly prepared and the Fe_2O_3 modified SBA-15c matrix is shown in Fig. 8. While the point of zero charge for the SBA-15c could be observed at a pH value of 1.5, the different iron oxide modified materials showed a zero charge point at pH values close to 2. These values are not only consistent with those found for similar systems in the literature [49, 50], but also indicate that at more basic pH conditions (values above 2), the surface of the adsorbent must have a negative net charge.

3.2 Adsorption tests

3.2.1 Effect of pH and the initial arsenic concentration

The adsorption of arsenic III on the prepared adsorbent materials in aqueous solutions was evaluated at pH values of 2 and 7. The arsenic was studied by varying the initial concentrations of arsenic at 5 and 10 ppm. According to the diagram published in the literature [51] on the speciation of arsenic in water as a function of pH and its redox potential, trivalent As would be present in the non-ionic form of arsenious acid H_3AsO_3 at both a pH of 2 and a value of 7. As seen in Fig. 9a, the prepared adsorbents performed better with a 3% ferric oxide load in a 5 ppm As(III) solution. The difference in adsorption capacity of the mentioned materials does not reach 10% when comparing both pH values, which makes sense since the arsenic species does not change at these values. Similar results were observed at an initial concentration of 10 ppm, as seen in Fig. 9b. This indicates that, for this form of inorganic arsenic, pH does not have a significant effect and that a 3% by weight concentration of Fe_2O_3 on the surface of the SBA-15c matrix appears to be optimal for further evaluations.

3.3 Adsorption kinetics

The adsorption kinetics of Arsenic III at an initial concentration of 0.5 ppm with the 3% Fe_2O_3/SBA-15c adsorbent were studied over a range of zero to 210 min, at a pH of 2 that matches with the isoelectric point of the material. The results of Fig. 10 show accelerated adsorption in the first 30 min, reaching 80% arsenic removal. However, the maximum adsorption capacity of trivalent arsenic was almost 90% in 90 min. The evaluation of the experimentally obtained data according to the selection process for the adsorption model published by Ho et al. [52], indicates that: (i) the system consists of nanoparticles whose charge will interact with the adsorbate, which will indicate an adsorption model controlled by reaction kinetics, and not by mass transfer processes, (ii) equilibrium is achieved quickly and in less than three hours, which also reveals a process controlled by kinetics and the data do not correspond to the evaluation on intraparticle diffusion, discarding a model controlled by the diffusion of the adsorbate in the adsorbent, and (iii) the data obtained fit better to a pseudo-first-order model, as can be seen in Fig. 10.

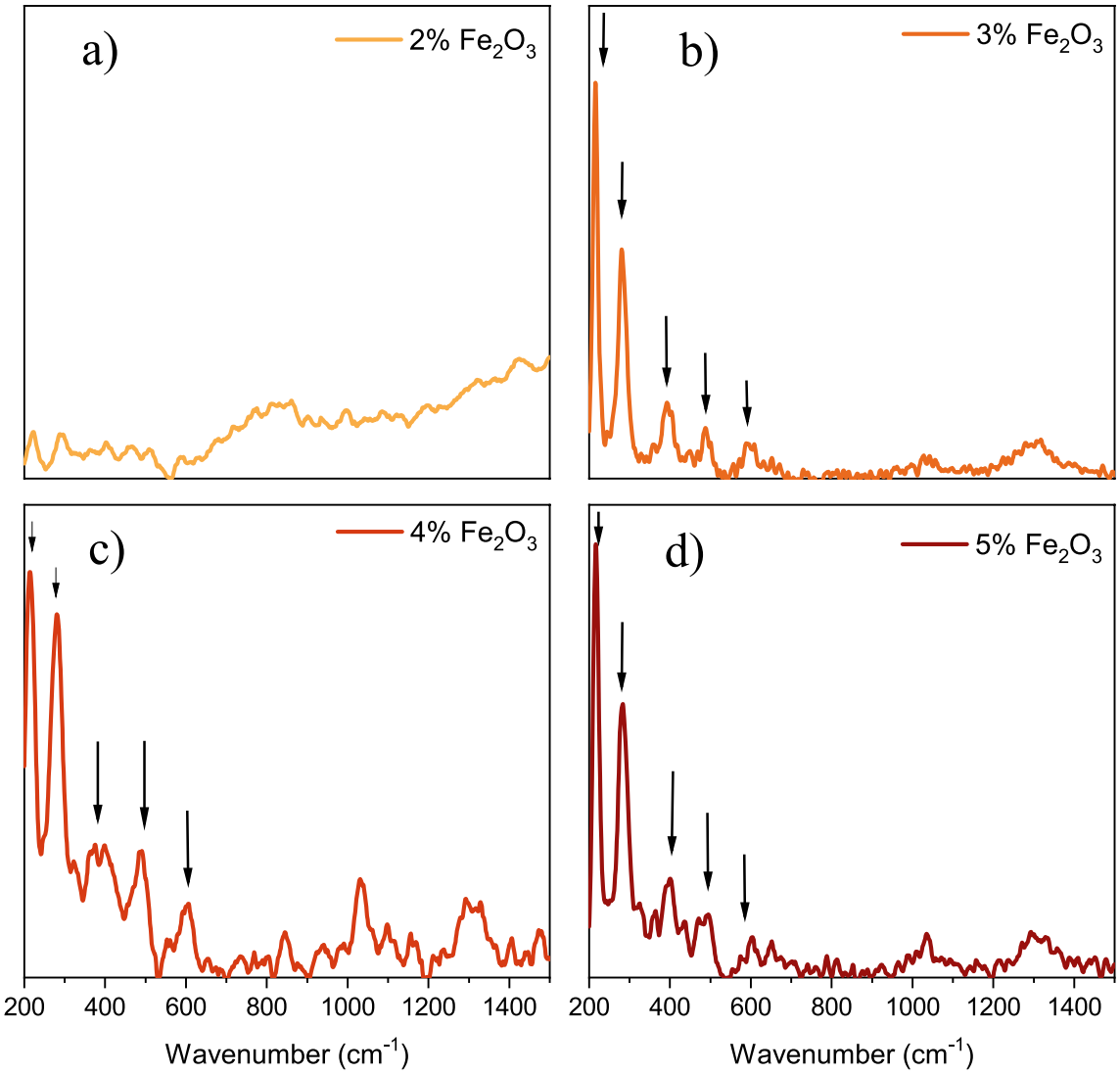

Fig. 7 Micro-Raman spectra for the adsorbent materials corresponding to hematite for 2.0 to 5.0 wt% Fe_2O_3, from **a** to **d** respectively. The arrows correspond to the phonon responses from the hematite

Table 3 Weight percentages of oxides present in the adsorbents

	Concentration (wt%)		
	SiO_2	Fe_2O_3	Cl
2%Fe_2O_3/SBA-15c	97.23	2.33	0.44
3%Fe_2O_3/SBA-15c	96.46	3.14	0.4
4%Fe_2O_3/SBA-15c	95.65	4.01	0.34
5%Fe_2O_3/SBA-15c	93.19	6.49	0.33

3.4 Adsorption models

The adsorption models proposed by Langmuir, Freundlich, and Redlich–Peterson were evaluated with the results of arsenic(III) adsorption, their adjustments are shown in Fig. 11. As can be seen, and in agreement with other iron-based systems for removing As(III) [53–55], the model that showed the best fit was Freundlich, slightly above the Redlich–Peterson model. The maximum adsorption capacity q_m was 0.94 mg/L and the fit reached a value of 0.836, according to the Langmuir model, while its K_L constant obtained a value of 0.041. The Freundlich model was adjusted with a correlation of 0.996 and calculated a value of the K_F constant of 6.855 and a value of 0.96 for the quotient 1/n. The Redlich–Peterson model was adjusted with a value of 0.992, similar to the Freundlich adjustment, which confirms that adsorption in this system does not follow monolayer coverage.

The response of the chemical bonds analyzed by infrared spectroscopy is shown in the spectrum of Fig. 12,

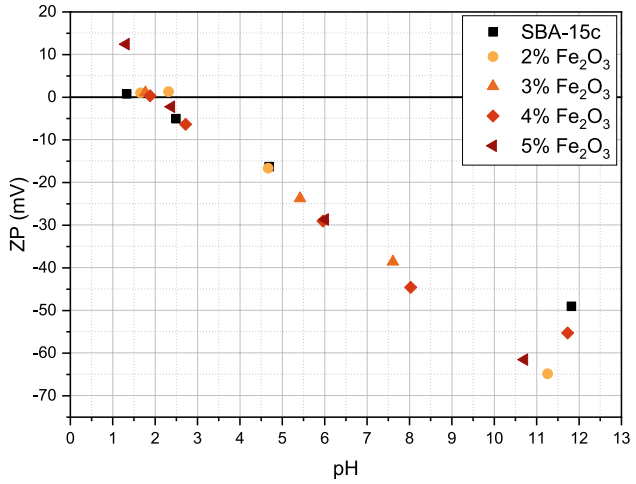

Fig. 8 Variations on the zeta potential of the SBA-15c matrix and adsorbents as a function of pH, ranging from acidic to basic values

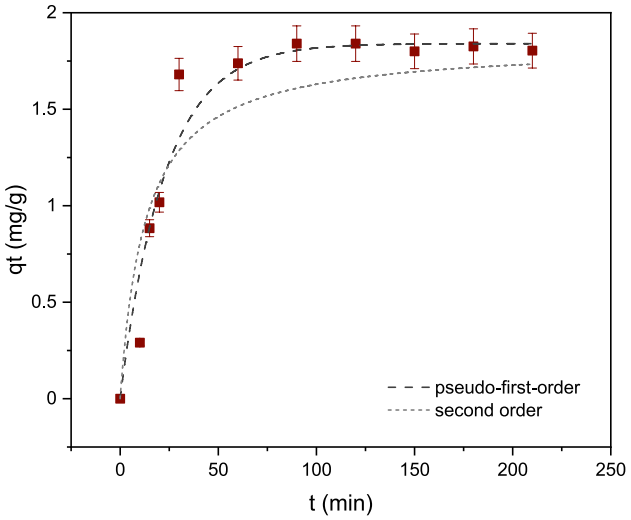

Fig. 10 Adsorption kinetics of As(III) on the 3%Fe_2O_3/SBA-15 adsorbent with an initial concentration of 5 ppm at 25 °C

which shows the transmittance of an adsorbent with a 3%Fe_2O_3 load supported on the mesoporous SBA-15c matrix before and after As(III) adsorption. The broad band around 3435 cm^{-1} corresponds to an H–O–H stretching band indicating the presence of hydrogen bonds and oxygen from water molecules in the materials. The band located at 969 cm^{-1} is related to the Si–OH stretching vibration [56].

Regarding iron oxide, the band at approximately 467 cm^{-1} corresponds to hematite due to its Fe–O bond [57], while the band at 1088 cm^{-1} may be related to metal hydroxides due to the formation of –FeOH complexes on the surface of the adsorbent. In addition, the band at 1631 cm^{-1} attributable to Fe–OH complexes is intensified after interaction with arsenic, in agreement with what is reported in the literature [58]. The accumulation of arsenic in the adsorbent can be identified by the pronounced peak at 800 cm^{-1}, which corresponds to the As–O stretching vibration [59].

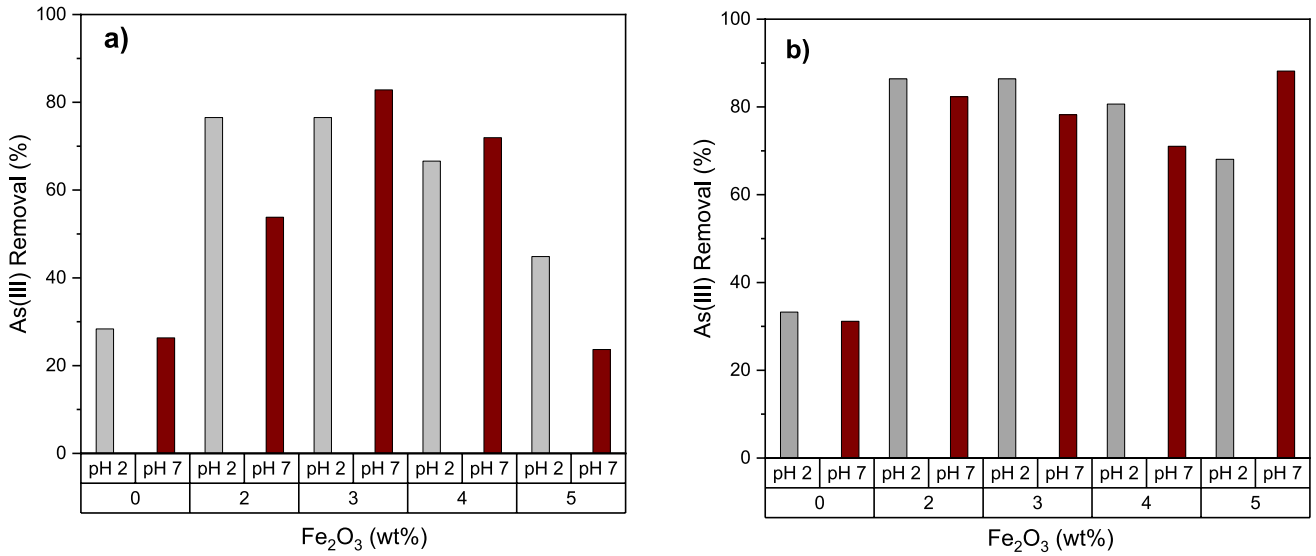

Fig. 9 Adsorption efficiencies of x%Fe_2O_3/SBA-15c for an aqueous solution of As(III) varying the initial pH of the solution, at a concentration of **a** 5 ppm, and **b** 10 ppm

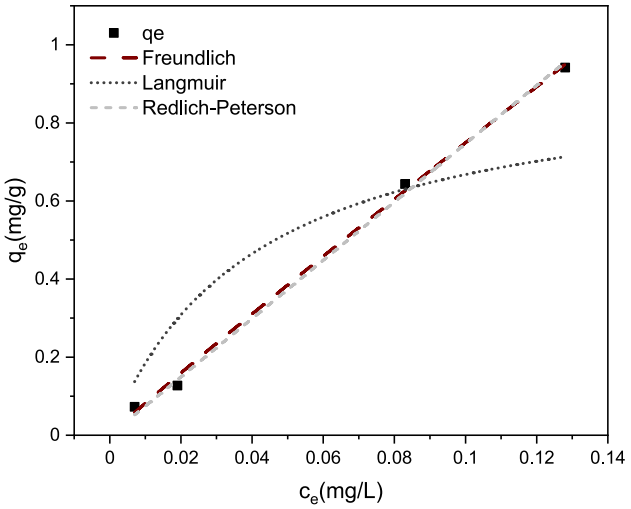

Fig. 11 Adjustments of the adsorption isotherms according to the Langmuir, Freundlich, and Redlich–Peterson models for the adsorption of arsenic on 3%Fe_2O_3/SBA-15c

4 Conclusions

The silica precursor to surfactant ratio of 1.55 resulted in a material with similar properties to SBA-15 particles but reduced in length. The STEM micrographs exhibited a reduction in the length of the material while conserving the size and arrangement of pores, in accordance with the SBET results. The hexagonal symmetry of the STEM images was corroborated by the low-angle X-ray diffraction results. The approach presented in this work provided information that conduces to further analysis to construct a solid explanation for the reduction in the length of the material. This modification led to a thermally stable particle with a higher surface area available to incorporate α-Fe_2O_3 nanoparticles. The pH of the solution played a central role in the performance of the adsorbents; for the low concentration of iron nanoparticles, the neutral values conducted greater adsorption capacities than the acidic values. The obtained adsorption isotherm indicates that the adsorption of As(III) on the surface of the ferric oxide adsorbent supported on the mesoporous SBA-15 matrix does not follow a monolayer coverage model on a homogeneous surface. Instead, the arsenic ions adhere to the Fe_2O_3 nanoparticles distributed in the matrix. In this context, the dispersion of the nanoparticles on an enhanced specific surface area represents a fundamental characteristic for improving the adsorbent's removal capacity in this system. The present study aimed to address and evaluate significant challenges during the adsorption of arsenic using a simple and cost-effective system. The discussed results demonstrated that by employing this material, it is possible to reduce the concentrations of arsenic in water to levels that meet environmental regulations.

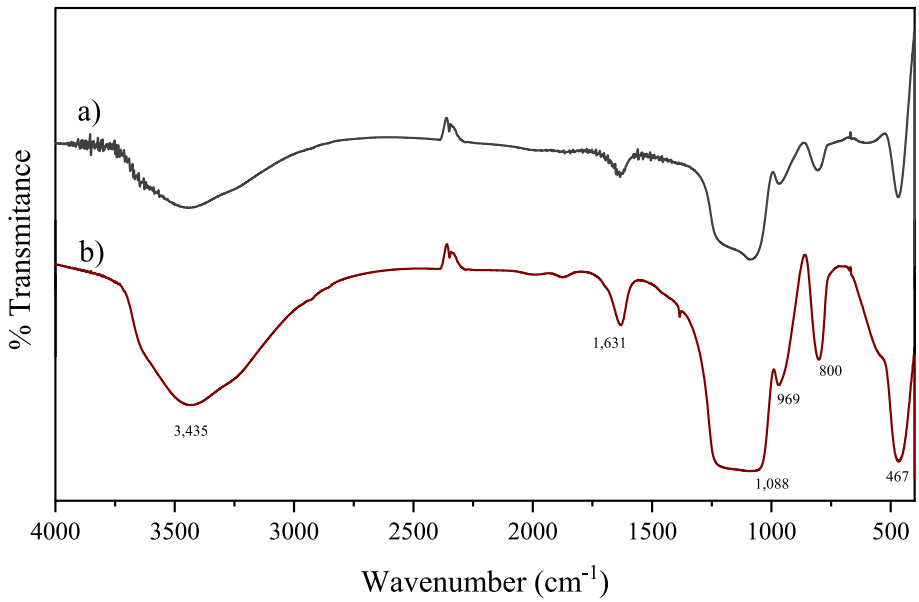

Fig. 12 FTIR spectra of the 3%Fe_2O_3/SBA-15c adsorbent: **a** before adsorption, and **b** after the adsorption of As(III)

Acknowledgements Viviana Palos-Barba acknowledges the Dirección General de Asuntos del Personal Académico DGAPA from the National Autonomous University of México UNAM for a postdoctoral scholarship. The authors acknowledge the Laboratorio Nacional de Caracterización de Materiales for material characterization.

Author contributions Study conception and design were performed by VPB, RNM, and EMRM. Material synthesis, data collection, and analysis were performed by VPB and MAF. Assistance in the laboratory was given by CPL and BMM. The manuscript was written by VPB, with all authors commenting on and approving the manuscript.

Funding Viviana Palos Barba—Postdoctoral Scholarship DGAPA-UNAM.

Declarations

Competing interests The authors have no conflicts of interest to declare that are relevant to the content of this article.

References

1. A. Baeyens, T. Goffin, Transforming our world: the 2030 Agenda for Sustainable Development. Eur. J. Health Law **22**(5), 35 (2015). https://doi.org/10.1163/15718093-12341375
2. D. Mayer-Foulkes, E. Serván-Mori, G. Nigenda, The sustainable development goals and technological capacity. Rev. Panam. Salud Publica **45**, 1–6 (2021). https://doi.org/10.26633/RPSP.2021.81
3. P.J. Landrigan et al., Pollution and global health—an agenda for prevention. Environ. Health Perspect. **126**(8), 3–8 (2018). https://doi.org/10.1289/EHP3141
4. C. Zamora-Ledezma et al., Heavy metal water pollution: a fresh look about hazards, novel and conventional remediation methods. Environ. Technol. Innov. **22**, 101504 (2021). https://doi.org/10.1016/j.eti.2021.101504
5. M.A. Armienta, N. Segovia, Arsenic and fluoride in the groundwater of Mexico. Environ. Geochem. Health **30**(4), 345–353 (2008). https://doi.org/10.1007/s10653-008-9167-8
6. L.M. Camacho, M. Gutiérrez, M.T. Alarcón-Herrera, M.L. Villalba, S. Deng, Occurrence and treatment of arsenic in groundwater and soil in northern Mexico and southwestern USA. Chemosphere **83**(3), 211–225 (2011). https://doi.org/10.1016/j.chemosphere.2010.12.067
7. C.C. Osuna-Martínez, M.A. Armienta, M.E. Bergés-Tiznado, F. Páez-Osuna, Arsenic in waters, soils, sediments, and biota from Mexico: an environmental review. Sci. Total Environ. **752**, 142062 (2021). https://doi.org/10.1016/j.scitotenv.2020.142062
8. D. Cauich-Kau, T.R. Rüde, A. Cardona-Benavides, J. Castro-Larragoitia, Natural occurrence and controls of arsenic in groundwater in a semiarid basin in the Mexican Altiplano. Hydrogeol. J. **30**(8), 2459–2477 (2022). https://doi.org/10.1007/s10040-022-02562-w
9. P.F. Scharp Cecilia, S. Hrachya, Mitigating arsenic in drinking water. *Unicef Policy Br. Mitigating Arsen. Drink. Water*, no. June, pp. 1–6 (2018).
10. M.T. Alarcón-Herrera et al., Co-occurrence, possible origin, and health-risk assessment of arsenic and fluoride in drinking water sources in Mexico: geographical data visualization. Sci. Total Environ. **698**, 134168 (2020). https://doi.org/10.1016/j.scitotenv.2019.134168
11. J.C. Bullen, L.N. Dworsky, M. Eikelboom, M. Carriere, A. Alvarez, P. Salaün, Low-cost electrochemical detection of arsenic in the groundwater of Guanajuato state, central Mexico using an open-source potentiostat. PLoS ONE (2022). https://doi.org/10.1371/journal.pone.0262124
12. M.Y.J. Baloch, S.A. Talpur, H.A. Talpur, J. Iqbal, S.H. Mangi, S. Memon, Effects of arsenic toxicity on the environment and its remediation techniques: a review. J. Water Environ. Technol. **18**(5), 275–289 (2020). https://doi.org/10.2965/JWET.19-130
13. UNICEF, *ARSENIC PRIMER Guidance on the Investigation & Mitigation of Arsenic Contamination*. (2018).
14. S. Vadahanambi, S.H. Lee, W.J. Kim, I.K. Oh, Arsenic removal from contaminated water using three-dimensional graphene–carbon nanotube-iron oxide nanostructures. Environ. Sci. Technol. **47**(18), 10510–10517 (2013). https://doi.org/10.1021/es401389g
15. A.R. Sari, A. Yulianingtias, R.A. Melinda, A. Mirwan, Removal of arsenic from synthetic acid mine drainage using Mn–Fe layered double hydroxide adsorbent. Jurnal Rekayasa Kimia & Lingkungan **16**(1), 45–51 (2021)
16. H. Sadeghpour, S. Ziaedin, F. Doulati, Environmental nanotechnology, monitoring & management arsenic removal by highly efficient $MnFe_2O_4/TiO_2/g\text{-}C_3N_4$ and $MnFe_2O_4/TiO_2$/GO adsorbents from a groundwater sample, Bardsir, Iran. Environ. Nanotechnol. Monit. Manag. **20**, 100821 (2023). https://doi.org/10.1016/j.enmm.2023.100821
17. M. Abdullah, G. Murtaza, M.A. Khan, Synthesis and characterizations of graphene/copper ferrite for efficient arsenic removal. Water. Air. Soil Pollut. (2023). https://doi.org/10.1007/s11270-023-06276-x
18. S. Mehanathan et al., Magnesium oxide nanoparticles for the adsorption of pentavalent arsenic from water: effects of calcination. Membranes **13**, 475 (2023)
19. F. Gamarra, J. Medina, W. Lanchipa, R. Tamayo, E. Sacari, Structural, optical, and arsenic removal properties of sol-gel synthesized Fe-doped TiO_2 nanoparticles. Nanomaterials (2022). https://doi.org/10.3390/nano12193402
20. K.F. Lam, K.L. Yeung, G. McKay, An investigation of gold adsorption from a binary mixture with selective mesoporous silica adsorbents. J. Phys. Chem. B **110**(5), 2187–2194 (2006). https://doi.org/10.1021/jp055577n
21. H. Takahashi, B. Li, T. Sasaki, C. Miyazaki, T. Kajino, S. Inagaki, Catalytic activity in organic solvents and stability of immobilized enzymes depend on the pore size and surface characteristics of mesoporous silica. Chem. Mater. **12**(11), 3301–3305 (2000). https://doi.org/10.1021/cm000487a
22. A. Vinu, V. Murugesan, O. Tangermann, M. Hartmann, Adsorption of cytochrome c on mesoporous molecular sieves: influence of pH, pore diameter, and aluminum incorporation. Chem. Mater. **16**(16), 3056–3065 (2004). https://doi.org/10.1021/cm049718u

23. B. Grünberg et al., Hydrogen bonding of water confined in mesoporous silica MCM-41 and SBA-15 studied by 1H solid-state NMR. Chemistry **10**(22), 5689–5696 (2004). https://doi.org/10.1002/CHEM.200400351
24. Y. Dong, B. Lu, S. Zang, J. Zhao, X. Wang, Q. Cai, Removal of methylene blue from coloured effluents by adsorption onto SBA-15. J. Chem. Technol. Biotechnol. **86**(4), 616–619 (2011). https://doi.org/10.1002/JCTB.2559
25. F. Suhail et al., Facile synthesis of hetaryl-modified MCM-41 and targeted removal of Pb(II) ions for water purification. J. Porous Mater. **27**(5), 1491–1504 (2020). https://doi.org/10.1007/s10934-020-00919-8
26. N. Fellenz et al., Chromium(VI) removal from water by means of adsorption-reduction at the surface of amino-functionalized MCM-41 sorbents. Microporous Mesoporous Mater. **239**, 138–146 (2017). https://doi.org/10.1016/J.MICROMESO.2016.10.012
27. W.I. Mortada, K.A. Nabieh, T.E. Helmy, Y.G. AbouEl-Reash, Microwave-assisted synthesis of MCM-41 composite with rice husk and its functionalization by dithizone for preconcentration of some metal ions from water and food samples. J. Food Compos. Anal. **106**, 104352 (2022). https://doi.org/10.1016/J.JFCA.2021.104352
28. Y. Song et al., Uptake of arsenic(V) using iron and magnesium functionalized highly ordered mesoporous MCM-41 (Fe/Mg-MCM-41) as an effective adsorbent. Sci. Total Environ. **833**, 154858 (2022). https://doi.org/10.1016/J.SCITOTENV.2022.154858
29. S. Cheng, Formation of platelet SBA-15 mesoporous materials studied by in-situ small-angle X-ray scattering. Mater. Chem. **20**, 46–49 (2009)
30. S.A. El-safty, T. Hanaoka, F. Mizukami, T. Aist, Design of highly stable, ordered cage mesostructured monoliths with controllable pore geometries and sizes. J. Phys. Chem. B (2005). https://doi.org/10.1021/jp050304d
31. D. Zhao, J. Sun, Q. Li, G.D. Stucky, S. Barbara, Morphological control of highly ordered mesoporous silica SBA-15. Chem. Mater. **12**, 275–279 (2000). https://doi.org/10.1021/cm9911363
32. R. Prucek et al., Ferrate(VI)-induced arsenite and arsenate removal by in situ structural incorporation into magnetic iron(III) oxide nanoparticles. Environ. Sci. Technol. **47**(7), 3283–3292 (2013). https://doi.org/10.1021/es3042719
33. S.R. Chowdhury, E.K. Yanful, A.R. Pratt, Arsenic removal from aqueous solutions by mixed magnetite–maghemite nanoparticles. Environ. Earth Sci. **64**(2), 411–423 (2011). https://doi.org/10.1007/s12665-010-0865-z
34. V. Kamath, P. Chandra, G.P. Jeppu, Comparative study of using five different leaf extracts in the green synthesis of iron oxide nanoparticles for removal of arsenic from water. Int. J. Phytoremed **22**, 1278–1294 (2020). https://doi.org/10.1080/15226514.2020.1765139
35. N. Torasso et al., Enhancing arsenic adsorption via excellent dispersion of iron oxide nanoparticles inside poly(vinyl alcohol) nanofibers. J. Environ. Chem. Eng. **9**(1), 104664 (2021). https://doi.org/10.1016/J.JECE.2020.104664
36. K. Flodström, V. Alfredsson, Influence of the block length of triblock copolymers on the formation of mesoporous silica. Microporous Mesoporous Mater. **59**(2–3), 167–176 (2003). https://doi.org/10.1016/S1387-1811(03)00308-1
37. O.B. Pagar, H.S. Nagare, Y.M. Chine, R.R. Autade, P.R. Narode, V.M. Sanklecha, Mesoporous silica : a review. Int. J. Pharm. Drug Anal. **6**(1), 1–12 (2018)
38. ISO [International Organization for Standardization], Determination of the specific surface area of solids by gas adsorption—BET method (ISO 9277:2010(E)). Ref. number ISO, 9277(9277), 30 (2010). https://doi.org/10.1007/s11367-011-0297-3
39. E.P. Barrett, L.G. Joyner, P.P. Halenda, The determination of pore volume and area distributions in porous substances. I. Computations from nitrogen isotherms. J. Am. Chem. Soc. **73**(1), 373–380 (1951). https://doi.org/10.1021/ja01145a126
40. ISO - ISO 17378-2:2014 - Water quality—determination of arsenic and antimony—Part 2: method using hydride generation atomic absorption spectrometry (HG-AAS).
41. K.S.W. Sing et al., Reporting physisorption data for gas/solid systems with special reference to the determination of surface area and porosity. Pure Appl. Chem. **4**, 603–619 (1985). https://doi.org/10.1351/pac198557040603
42. F. Schüth, K.S.W. Sing, J. Weitkamp, *Handbook of Porous Solids*, vol. 1 (Wiley, Weinheim, 2002)
43. L.B. McCusker, F. Liebau, G. Englehardt, Nomenclature of structural and compositional characteristics of ordered microporous and mesoporous materials with inorganic hosts (IUPAC recommendations 2001): physical chemistry Division commission on colloid and surface chemistry including catalysis. Microporous Mesoporous Mater. **58**(1), 3–13 (2003). https://doi.org/10.1016/S1387-1811(02)00545-0
44. M. Ulfa, A.M. Jannah, Synthesis of mesoporous Fe_2O_3/SBA-15 and its application for nickel(II) ion adsorption. Orient. J. Chem. **34**(1), 420–427 (2018). https://doi.org/10.13005/ojc/340145
45. D. Zhao et al. Triblock Copolymer Syntheses of Mesoporous Silica with Periodic 50 to 300 Angstrom Pores. vol. 109, (1995).
46. B. Chen, G. Quan, Y. Dong, Increasing the oral bioavailability of poorly water- soluble carbamazepine using immediate-release pellets supported on SBA-15 mesoporous silica. (2012). https://doi.org/10.2147/IJN.S37650
47. A. Lassoued, B. Dkhil, A. Gadri, S. Ammar, Control of the shape and size of iron oxide (a-Fe_2O_3) nanoparticles synthesized through the chemical precipitation method. Results Phys. **7**, 3007–3015 (2017). https://doi.org/10.1016/j.rinp.2017.07.066
48. A. M. Jubb and H. C. Allen, Vibrational spectroscopic characterization of hematite, maghemite , and magnetite thin films produced by vapor deposition. (2010). https://doi.org/10.1021/am1004943.
49. S. Mahouche-chergui, Y. Grohens, E. Balnois, B. Lebeau, and Y. Scudeller, Adhesion of silica particles on thin polymer films model of flax cell wall. (2014). https://doi.org/10.4236/msa.2014.513097.
50. X. Yu, S. Tong, M. Ge, J. Zuo, C. Cao, and W. Song, One-step synthesis of magnetic composites of cellulose @ iron oxide nanoparticles for arsenic removal. pp. 959–965 (2013). https://doi.org/10.1039/c2ta00315e.
51. I.A. Katsoyiannis, A.I. Zouboulis, Comparative evaluation of conventional and alternative methods for the removal of arsenic from contaminated groundwaters. Rev. Environ. Health **21**(1), 25–41 (2006)
52. Y.S. Ho, J.C.Y. Ng, G. McKay, Kinetics of pollutant sorption by biosorbents: review. Sep. Purif. Methods **29**(2), 189–232 (2000). https://doi.org/10.1081/SPM-100100009
53. J.C. Moreno-Piraján, L. Giraldo, Activated carbon from bamboo waste modified with iron and its application in the study of the adsorption of arsenite and arsenate. Cent. Eur. J. Chem. **11**(2), 160–170 (2013). https://doi.org/10.2478/s11532-012-0138-7
54. Z. Ren, G. Zhang, J. Paul Chen, Adsorptive removal of arsenic from water by an iron-zirconium binary oxide adsorbent. J. Colloid Interface Sci. **358**, 230–237 (2011). https://doi.org/10.1016/j.jcis.2011.01.013
55. S. Kundu, A.K. Gupta, Arsenic adsorption onto iron oxide-coated cement (IOCC): regression analysis of equilibrium data with several isotherm models and their optimization. Chem. Eng. J.

122(1–2), 93–106 (2006). https://doi.org/10.1016/j.cej.2006.06.002
56. M. Tadic et al., Magnetic properties of hematite (a-Fe_2O_3) nanoparticles synthesized by sol-gel synthesis method: the influence of particle size and particle size distribution. J. Electr. Eng. **70**, 71–76 (2019). https://doi.org/10.2478/jee-2019
57. N. Khorshidi, A.R. Azadmehr, Competitive adsorption of Cd(II) and Pb(II) ions from aqueous solution onto iranian hematite (Sangan mine): optimum condition and adsorption isotherm study. Desalin. Water Treat. **2018**(58), 106–119 (2017). https://doi.org/10.5004/dwt.2017.0038
58. R.R. Devi et al., Removal of iron and arsenic(III) from drinking water using iron oxide-coated sand and limestone. Appl. Water Sci. **4**(2), 175–182 (2014). https://doi.org/10.1007/s13201-013-0139-5
59. V. Jadhav, S. Sachar, S. Chandra, D. Bahadur, P. Bhatt, Synthesis and characterization of arsenic trioxide nanoparticles and their in vitro cytotoxicity studies on mouse fibroblast and prostate cancer cell lines. J. Nanosci. Nanotechnol. **16**(7), 7599–7605 (2016). https://doi.org/10.1166/jnn.2016.11663